Effect of Laser Energy Density on Surface Morphology, Microstructure, and Magnetic Properties of Selective Laser Melted Fe-3wt.% Si Alloys

Shuohong Gao, Xingchen Yan, Cheng Chang, Eric Aubry, Min Liu, Hanlin Liao, and Nouredine Fenineche

To study the effect of the laser energy density (LED) on surface morphology, microstructural evolution, and magnetic properties of Fe-3wt.% Si alloy, the alloy was manufactured via selective laser melting (SLM) technology. The SLM Fe-3wt.% Si parts were characterized by a series of advanced material methods including a 3D profilometer, optical microscope, scanning electron microscopy, and vibrating sample magnetometer, etc. The results show that no obvious microcracks exist in the SLM Fe-3wt.% Si parts. With the LED increases, the porosity rate and the surface roughness of the SLM Fe-3wt.% Si parts decrease. Furthermore, the cross-sectional microstructure of the SLM Fe-3wt.% Si parts is a typical columnar structure with an orientation growth building direction. The microhardness of each SLM Fe-3wt.% Si sample is higher than 200 $HV_{0.1}$. Besides, the coercivity of SLM Fe-3wt.% Si parts decreases first and then increases with the increase in the LED. The specimen with a LED at 300 J/m exhibits better comprehensive magnetic properties than others. It could be concluded that the magnetic properties of SLM Fe-3wt.% Si alloys are affected by the synergistic effects of manufacturing defects and internal stress.

1. Introduction

Soft magnetic materials are regarded as a type of materials that are easy to be magnetized and demagnetized (Ref 1), such as, Fe-Ni, Fe-Co, Fe-Si alloys. Owing to the high permeability, low coercivity, and low hysteresis loss, soft magnetic materials are widely used in the magnetic field (Ref 2). Silicon steel, an iron-based alloy with Si element in concentrations between 2 and 7wt.%, is a quite significant class of the soft magnetic materials (Ref 3). Within the family of silicon steel, due to high magnetic transition temperature and low electrical resistivity, Fe-3wt.% Si soft magnetic alloy was attracted extensive attraction in many industrial applications including sensors, transformers, inductive devices, electric motors, etc. (Ref 4). Traditionally, the silicon steel is fabricated via an extrusion process or multiple rolling processes followed by an annealing heat treatment (Ref 5). Unique forming processes of silicon steel have been reported in many studies including powder metallurgy (Ref 6), cast strips (Ref 7), and electron-beam physical vapor deposited (Ref 8). Even if these methods have been investigated in the past decades, they are rarely used in commercial applications.

Additive Manufacturing (AM) technology is a material processing method which bases on computer-aided design (Ref 9). AM products are fabricated via a layerwise method utilizing software and numerical control system, including extrusion, sintering, melting, photocuring, spraying, etc. Because of the freedom of unrivaled design, AM technologies have been widely applied for the fabrication of metal, plastic, and ceramic materials (Ref 10). Selective laser melting (SLM) is a kind of AM technology using a laser beam as the energy input. During the SLM process, rapid solidification (10^3-10^6 K/s) can result in an ultra-fine microstructure (Ref 11). Therefore, SLM technology plays a vital role in the extended potential applications for manufacturing high-performance alloys. In the automotive, medical, and aerospace industries, SLM technology has been applied in the fabrication of high-quality metallic structural parts with brilliant properties (Ref 12). Apart from the structural applications, the SLM also has great potential in the production of functional parts such as soft magnetic alloys (Ref 13).

So far, the investigations for the fabrication of Fe-based soft magnetic alloys by SLM have been focused on Fe-Ni and Fe-Si alloys. Zhang et al. (Ref 14, 15) have investigated the SLM

Shuohong Gao and **Xingchen Yan**, ICB UMR 6303, CNRS, Univ. Bourgogne Franche-Comté, UTBM, 90010 Belfort, France; and National Engineering Laboratory for Modern Materials Surface Engineering Technology, The Key Lab of Guangdong for Modern Surface Engineering Technology, Institute of New Materials, Guangdong Academy of Sciences, Guangzhou 510651, P.R. China; **Cheng Chang**, ICD-LASMIS, UMR CNRS 6281, University of Technology of Troyes, 12 rue Marie Curie, CS 42060, 10004 Troyes Cedex, France; **Eric Aubry**, Nipson Technology, 90000 Belfort, France; and **Min Liu**, National Engineering Laboratory for Modern Materials Surface Engineering Technology, The Key Lab of Guangdong for Modern Surface Engineering Technology, Institute of New Materials, Guangdong Academy of Sciences, Guangzhou 510651, P.R. China; **Hanlin Liao** and **Nouredine Fenineche**, ICB UMR 6303, CNRS, Univ. Bourgogne Franche-Comté, UTBM, 90010 Belfort, France. Contact e-mail: yanxingchen@gdinm.com.

processed Fe-Ni alloys using the mixed powders of Fe-30%wt Ni, Fe-80%wt Ni as raw materials, SLM process seems to be suitable for their fabrication. Magnetic properties can be improved by parameter optimization. It is better than the Fe-30%wt Ni alloy fabricated by laser engineered net shaping. According to the study of Mikler et al. (Ref 16), it can be noted that balling mixed powders would lead to the microstructure and elemental segregation in the SLMed alloys. Additionally, Garibaldi et al. (Ref 17, 18) analyzed the relationship between parameters, microstructures, and magnetic properties of the SLM processed Fe-6.5%wt.Si alloy. The results indicated that the soft magnetic component with complex morphology could be fabricated by this method. Safia Alleg et al (Ref 19) prepared the SLM Fe-Si-B soft magnetic parts using $Fe_{922.4}Si_{3.1}B_{4.5}$ alloy powder. The results have shown that the variation of their microstructure and magnetic properties was closely related to the laser scanning rate. Thus, appropriate SLM processing parameters are essential for the preparation of soft magnetic alloys. Recently, Plotkowski et al. (Ref 20) reported the influence of scan pattern and geometry on the microstructure and soft-magnetic performance of Fe-3wt.% Si using a Renishaw AM250 system. It was found that thin wall geometries maybe have lower power losses than others, which is attributed to their effective limit of the development of eddy current. However, they did not systematically report the effect of SLM process parameters on the surface morphology and microstructures of Fe-3wt.% Si alloys. As mentioned above, Fe-based soft magnetic alloy produced through SLM has attracted much attention. However, the research about the SLM Fe-3wt.% Si alloy is relatively scarce. Notably, laser energy density (LED), a direct and significant factor, has an extremely significant impact on the microstructure and magnetic properties of soft magnetic alloys.

Additionally, the investigations about Fe-Si soft magnetic alloys processed via SLM technology were also rare, especially the study on SLM Fe-Si alloy using the metallurgical powder as raw materials. Therefore, this work focused on the systematical investigation for optimizing the processing of SLM Fe-3wt.% Si alloy, to improve the microstructures and the properties of SLM Fe-Si soft magnetic alloys, and to promote the development of their industrial applications. The effect of the LED on surface morphology, the microstructures and magnetic properties of SLM Fe-3wt.% Si alloy was explained in detail.

2. Materials and Methods

2.1 Powder Characterization

In this work, Fe-3wt.% Si alloy powder was used as the raw material. The powder was purchased from POCO Holding CO., LTD (Shenzhen, China). Shape, morphology, and chemical composition of the powder were characterized by scanning electron microscopy (SEM JEOL-5900 LV, Japan). The particle size distribution of the powder was measured by a laser diffraction powder sizer (Mastersizer 2000, Malvern Instruments Ltd., UK). Besides, the overview and representative magnified morphology of the used metallurgical powder are presented in Fig. 1(a). The powder particles were mainly spherical and near-spherical in shape, without satellite particles on the surface. That is an important characteristic of excellent flowability which meets exactly the requirement during the

SLM process. The particle size distribution is displayed in Fig. 1(b). $D_V(10)$, $D_V(50)$, and $D_V(90)$ of the powder are 16.2 µm, 37.7 µm, and 79.1 µm, respectively. And the result of EDS characterization is shown in Fig. 1(c), it can be confirmed that the content of silicon is about 3% (wt).

2.2 SLM Sample Preparation

A series of cubic specimens with dimensions of 8 mm × 8 mm × 8 mm were prepared using a selective laser melting machine MCP Realizer SLM 250 system (MCP-HEK Tooling GmbH, Germany). It was equipped with an Nd-YAG fiber laser. As described in Fig. 2, a zigzag scanning pattern with the neighboring laser track rotation of 90° was utilized during the SLM process. Five different laser powers (P, W) with 50 W, 70 W, 100 W, 140 W, 180 W were used to prepare a series of SLM cubic samples. The laser spot (µm), laser scanning speed (V, m/s), hatch distance (µm), and layer thickness (µm) were kept in a constant value with 35 µm, 0.33 m/s, 60 µm, and 30 µm, respectively. To avoid oxidation, the chamber was adopted under an argon atmosphere to maintain the content of residual oxygen content below 1.0 %. Moreover, the LED (E, J/m) was calculated via the equation as a linear function of the scanning speed and laser power:

$$E = \frac{P}{V}$$

and the specimens named hereafter E150, E210, E300, E420, and E540 according to E = 150, 210, 300, 420, and 540, respectively.

2.3 Sample Characterization

The roughness and surface morphology of the top side (XY plane) of all SLM samples were investigated by a DektakXT profilometer (Bruker, American) and an SEM system. These SLM samples were embedded in resin, polished, and then etched in a Nital solution (3% nitric + 97% ethanol) for 30-40 s. An optical microscope (OM, Leica) was used to obtain optical micrographics and observe the microstructure characteristics. The relative porosity was determined from the OM micrographs by an image analysis method. To achieve repeatability, the XZ plane of each sample was analyzed with a minimum of five optical micrographs at different areas alternatively via the image processing software ImageJ. An SEM system was employed to evaluate the feature of the microstructures. The Vickers hardness measurements were carried out at different locations on the XY and XZ plane, respectively. The Vickers hardness was measured using a microhardness tester (Leiz-Wetzlar, Germany) at a condition with a load of 100 g and an indentation time of 25 s. To ensure accuracy, the average value of the hardness was recorded by 10 measurements. The magnetic properties with coercivity and saturation magnetization of SLM specimens were evaluated by a vibrating sample magnetometer (VSM) at room temperature.

3. Results and Discussion

3.1 Macroscopic Morphology

Surface morphology is an important feature of SLM products, which can reflect manufacturing quality. To investi-
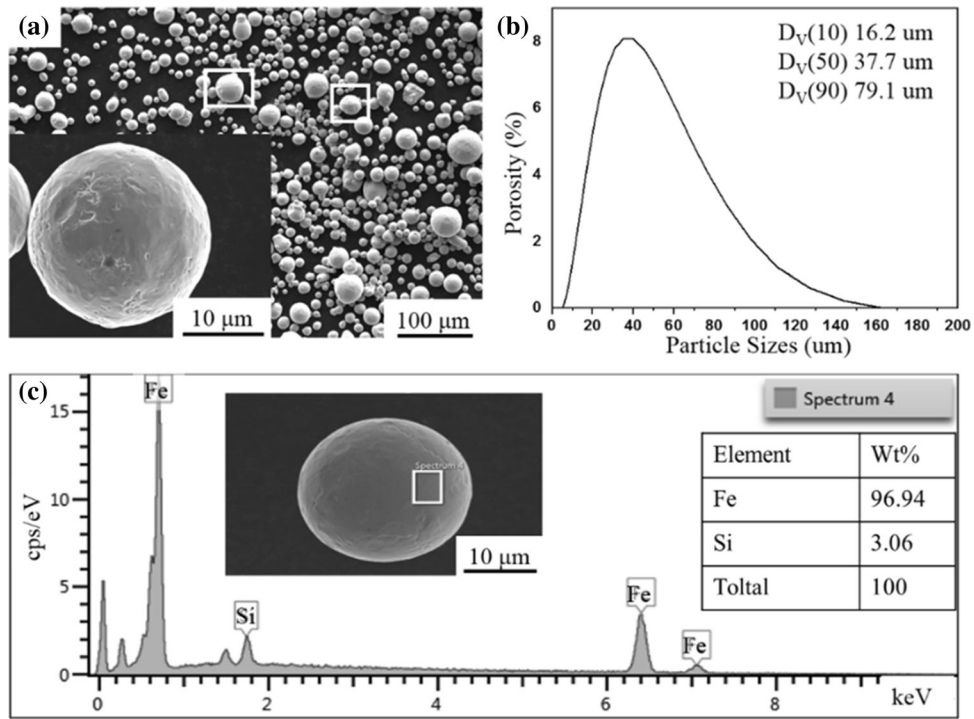
Fig. 1 Characterization of the feedstock powder. (a) SEM images of the morphology; (b) particle size distribution; (c) EDS results of chemical composition
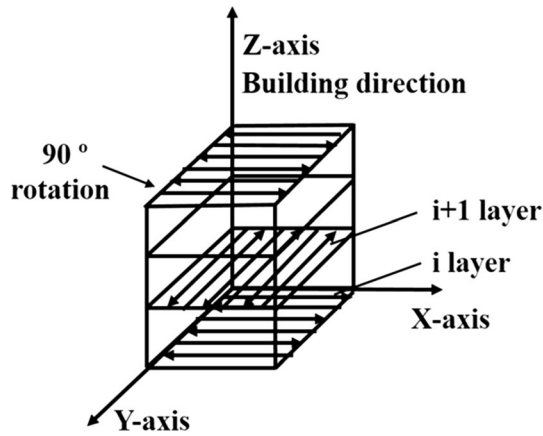

Fig. 2 SLM scanning strategy

gate the influence of LED on surface morphology, the top surface (XY plane) of SLM Fe-3wt.% Si alloy was characterized. The macroscopic surfaces of the corresponding samples are shown in Fig. 3(a). As displayed in Fig. 3(b), (c), (d), (e), and (f), with various LEDs, the SEM surface macroscopic morphology images of different specimens were obtained. Although the spattering particles are almost found on the surface of all specimens, significant distinctions with different melt pools and laser track patterns (marked by orange lines in Fig. 3(d) and (e)) are still observed. Under low LED, not only some spherical shape particles but also irregular protuberances (marked by white arrows in Fig. 3(b) and (c)) can be observed on the surface of samples E150 and E210. The laser tracks on the surface of these samples are incomplete and discontinuous with a curved geometry, which is the result of a segmentation effect on the elongated melt pool. The reasons for these

phenomena would be summarized by the following aspects. On one side, during the SLM process, some powder particles could not be fully melted due to the low temperature of the laser spot with low LED. In this situation, those un-melted particles were left on the surfaces. On the other hand, the physical model for the surface tension of liquid metal mainly contains a normal component and tangential component of surface, low LED that had a low temperature which would lead to the high tension of both normal and tangential components (Ref 21-23). The melting powder would shrink into spherical particles due to the high surface tension, which leads to the formation of a series of discrete molten pools and several irregular protuberances. It is defined as balling effect (Ref 24). Additionally, the balling effect occurred when the melted powder did not wet the underlying layer due to oxide contamination of the layer on the substrate and the surface of the melt. Besides, an insufficient heat transmission will also lead to a failure spreading of the laser tracks, which results in the clearance leakage between the adjacent laser tracks. It would cause the formation of the void. With the increase in LED, the laser tracks are gradually clear, completed a regular pattern. And the adjacent laser tracks are also closely connected. Meanwhile, there are a few fine particles marked by white arrows in Fig. 3(f) on the surface of sample E540 at the highest LED with 540 J/m. Some of them are the general spattering particles, and others are special spattering particles, i.e., over-burning debris caused by excessive LED (Ref 25).

It is well known that the roughness is an important index to evaluate the surface quality of SLM products. It has a direct relationship between the roughness with the surface morphology. To understand the impact of the LED on the surface roughness of the SLM Fe-3wt.% Si alloy, the three-dimensional surface topographies and surface roughness (Ra) were further analyzed by a profilometer. As represented in Fig. 4(a), (b), (c),
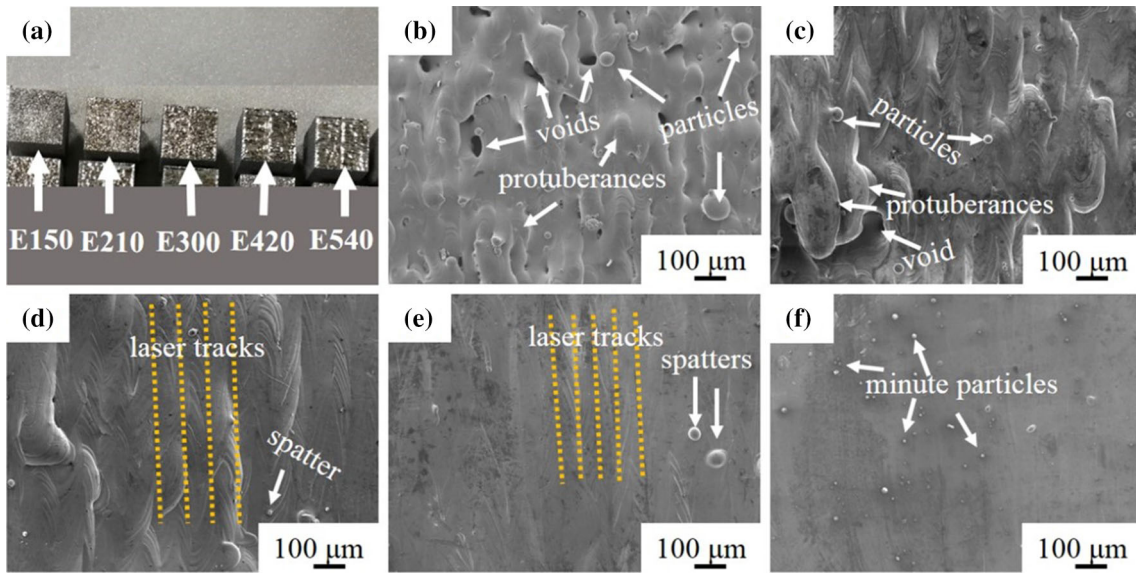
Fig. 3 Macroscopic morphology and SEM images of surface morphology of SLM samples at different LED. (a) Macroscopic morphology of the SLM samples. (b) 150 J/m, (c) 210 J/m, (d) 300 J/m, (e) 420 J/m, (f) 540 J/m
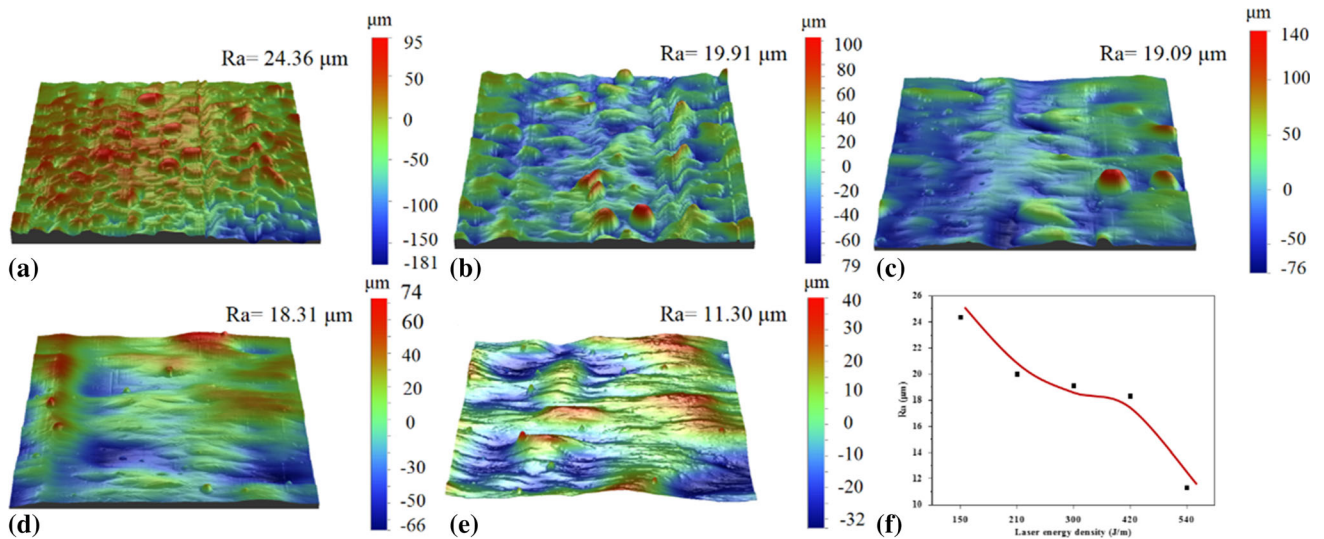

Fig. 4 Three-dimensional surface topographies and the values of roughness of the SLM parts at different LED. (a) 150 J/m, (b) 210 J/m, (c) 300 J/m, (d) 420 J/m, (e) 540 J/m, (f) the values of roughness

(d), and (e), the three-dimensional surface topographies of the SLM parts are consistent with the morphology under SEM (Fig. 4(b), (c), (d), (e) and (f)). The surface macroscopic morphologies present a phenomenon of gradual smoothing with the increase in LED. In Fig. 4(f), it can also be reflected that the variation in surface roughness decreases as the increase in LED. In fact, the balling effect (Ref 26) and the spattering phenomenon (Ref 27) are the primary factors affecting the surface roughness of the SLM parts. At low LED, the liquid phase is insufficient which leads to poor fluidity of the powder and short lifetime of the molten pool, contributing to the formation of the balling effect (Ref 26). As it can be seen in both Fig. 3 and 4, with the increase in LED, the effect of the balling becomes gradually less prominent. Meanwhile, high LED (≥ 300 J/m) per unit area that leads to parts of spattering particles are melted through intensive heat transfer (Ref 27). In

high LED, the number of spattering particles is less and their size is smaller. All these contribute to the decrease in surface roughness (24.36–11.30 μm) of the samples with the increase in LED. The roughness of the top surface is strongly dependent on LED, which can be proved by the mentions above. It can be concluded that the surface roughness of the SLM parts decreases with the decrease in LED. Insufficient energy density causes a rough surface and obvious voids, but excessive energy density leads to overburning.

3.2 Microstructural Analysis

3.2.1 Manufacturing Defects. It is well known that the SLM parts have two main internal defects: cracks and pores. They can be observed by an optical microscope (Ref 28). This part aims to describe the impact of LED on the internal defects

of Fe-3wt.% Si alloys produced by SLM. The internal quality could mostly be reflected in the cross-sectional plane (parallel to building direction) of SLM products. And the cross-sectional (XZ plane) OM images of SLM Fe-3wt.% Si parts are demonstrated in Fig. 5(a) (b), (c), (d) and (e). It is noted that macrocracks are not obvious in all samples, only some pore defects were observed. The absence of microcracks benefits the performance of SLM products. Moreover, it could be seen that the number of pores in the sample decreases with the increase in LED. In the meantime, it is found that only some small pores with regular shapes are observed in the sample E540, but both large pores with irregular shapes and small pores with regular shapes are observed in the other samples (as shown in Fig. 5, which are highlighted by different symbols). And both the size and the number of large pores decrease with the increase in LED.

The large pores mentioned above are identified as keyholes (marked by white arrows) due to their irregular shape and their larger size above 100 μm, while the small pores are identified as gas pores (marked by orange circles) according to their size smaller than 100 μm with spherical shapes (Ref 29, 30). The formation of keyholes is attributed to rapid solidification of the metal powder without complete filling, leading to gaps and balling effects on the surface of layers in the SLM processing. Especially, a low LED reducing the operative temperature within molten pools, resulting in a limited amount of liquid within molten pools and a restriction of complete spreading of the liquid powder. And the previous layers could not be re-melted totally in this case (Ref 31). And the balling effects on the surface of each layer were also serious at low laser energy laser input. Accordingly, keyholes with large size could be obtained in adjacent layers because of the above comprehensive reasons. It was explained in the previous section: as the increase in LED, the solidification time can be extended. In the process of SLM, not only the spreading of the liquid metal was improved, but also the balling phenomenon became weak. For these reasons, both size and number of large pores decrease with the increase in LED. Gas pores can be created by two types of gases that existed during the SLM processing. One is trapped within the melt pool, the other is from the powder during consolidation (Ref 30). During SLM processing, turbulent flow is formed in molten pools with strong gas rolling due to a high energy density (Ref 28). To a certain extent, the increase in the LED might lead the dynamics of Marangoni which affects the increase in the possibility of pores formed in the solidified molten pools (Ref 32). However, it can also promote the ability of gas rolling and escaping from the molten pools, which can reduce the pores and increase the densification at a high level (Ref 23). As displayed in Fig. 5(f), it can be also proved that the internal porosity of the samples would decrease with the increase in LED. Additionally, the reduction in the porosity rate is the largest when the LED increases from 150 J/m to 240 J/m. With increasing the LED from 240 to 300 J/m, the porosity decreases significantly until lower than 1%. A further increase in LED can result in the evaporation and burning of elements, which causes the formation of a few pores (Ref 33). Thence, the internal porosity rate of E420 and E540 samples is approximative, while it is still lower than 1%. The internal manufacturing defects at low LED are irregular pores but near-circular pores at high LED. Under the suitable LED, no cracks can be observed and the porosity is lower than 1%, which improve significantly the properties of the SLM parts.

3.2.2 Microstructural Evolution. The internal microstructure of the soft magnetic alloy is quite significant for its properties, especially its magnetic properties. And the microstructure of the alloy produced by SLM is not only affected by its material composition but also strongly related to the parameters during the SLM fabrication process. The defects of the SLM products can be generally divided into porosity and cracks, which have been described in the previous analysis of porosity. However, in a further OM observation of etching samples, it can be found clearly that un-melted particles (indicated by yellow arrows) were also one of the defects in the SLM samples (Ref 34) because un-melted powders are usually spherical shapes and in dendritic phases. After etching, the corresponding microstructures of the XY plane of SLM Fe-
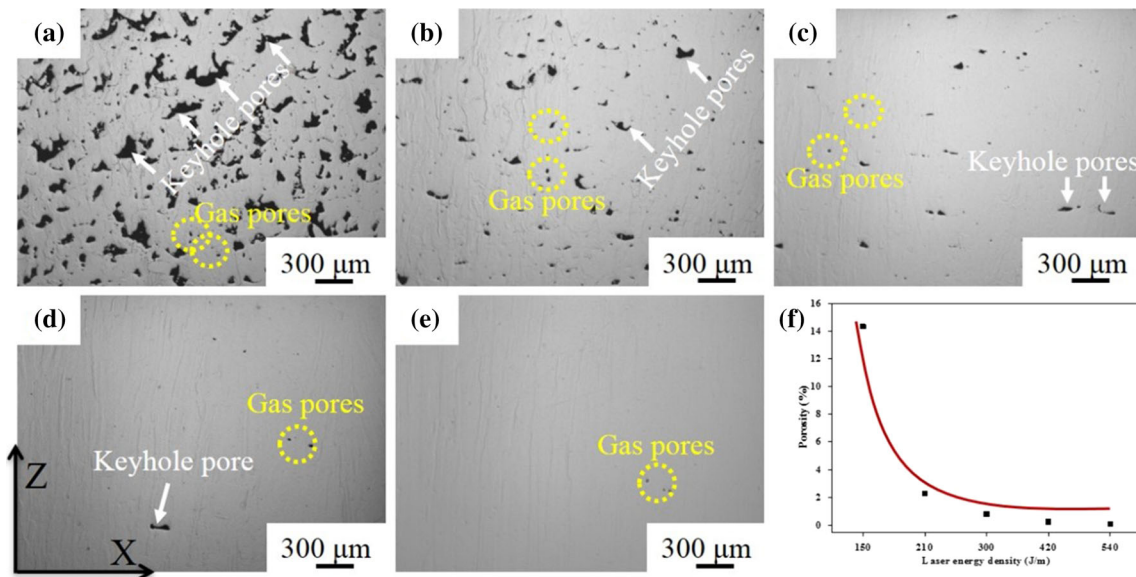

Fig. 5 OM images of cross-sectional (XZ plane) at different LED and porosity rate of SLM specimens at different LED. (a) 150 J/m, (b) 210 J/m, (c) 300 J/m, (d) 420 J/m, (e) 540 J/m, (f) porosity rate changes as a function of laser energy density
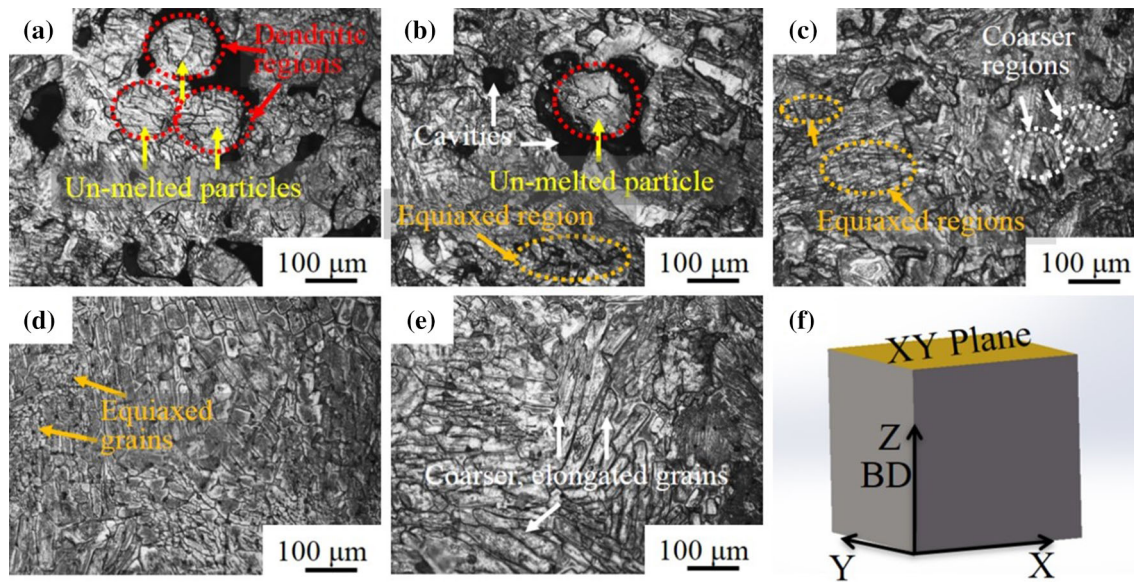
Fig. 6 OM images (XY plane) of the SLM parts at different LED and 3D physical model of the sample. (a) 150 J/m, (b) 210 J/m, (c) 300 J/m, (d) 420 J/m, (e) 540 J/m, (f) 3D physical model of the sample

3wt.% Si alloys are presented in Fig. 6. It is identified clearly that there are un-melted particles in E150 and E210 samples at low LED. And some obvious cavities (indicated by white arrows) are found around these un-melted particles, resulting in a microstructural discontinuity. As discussed, the LED plays a significant role in determining the amount and magnitude of such un-melted particles (Ref 24, 35). Un-melted particles come from a lack of fusion, that's to say the input energy was not enough to melt the whole powders, which led to an unstable molten pool. A lack of fusion presents large cavities around un-melted particles, which is due to the poor bonding between the melt pools or laser tracks (Ref 36, 37). Although a few pores can be observed in the sample E300, neither un-melted particles can be found, nor in other samples (E420, E540). It can be indicated that all powder particles can be almost melted completely when the LED exceeds 300 J/m.

Moreover, a few equiaxed regions (indicated by orange circles and arrows) are found besides some regions of dendritic grains in the samples E150 and E210 at low LED, while no regions of coarser, elongated grains (indicated by white circles and arrows) were identified clearly. However, when the LED was 300 J/m, in the sample E300, the microstructure consists of mainly equiaxed grains and coarser grains. With the increase in LED, the grain boundaries on the surface are visible and appear significantly. Furthermore, the microstructures are more homogeneous and regular. The regions of equiaxed grains and coarser elongated grains are observed clearly in the samples E420 and E540 with high LED. With comparing samples E150 and E300, it could be noticed that increasing the LED promotes columnar grain formation. These phenomena also occurred when the LED is increased from 400 to 1000 W in the literature (Ref 38). According to the report of Michele Garibaldi (Ref 18), when the LED was doubled, the increasing dependency of morphological and crystallographic texture on SLM parts could be noted remarkably. Therefore, the correlation between LED and grain formation could be explained by the increasing amount of partial re-melting and the enhancing smoothness of the deposited layers. Unfortunately, due to the Marangoni

effects and over burning, some black particles also appear in samples E420 and E540.

Similarly, the OM micrographs in Fig. 7 provide insights into the microstructural features of corresponding samples at different LEDs for the XZ plane (the microstructures for the XZ plane of the samples were also found for the YZ plane and are therefore not shown here). Their regular pattern of structural evolution was found equivalent to the XY plane of the previously analyzed. With the increase in LED, the microstructures of specimens become denser, and the boundaries of grains clearer and easier to be recognized. When E ≥ 300 J/m, the obvious and overall columnar structures oriented along the building direction are identified clearly in the corresponding samples. According to the fundamentals of solidification, a grain selection process in which grains whose "easy growth" directions (the $<001>$ family for the bcc system) are oriented along the direction of solidification (Ref 18, 39). For this reason, it is concluded that the epitaxial growth of the grains accrued at high LED.

Furthermore, it is observed that fine equiaxed structures usually appear in the areas between the coarse columnar structures. Moreover, the proportion of coarse columnar structures is the largest when E = 500 J/m. Those microstructures of the XZ plane could correspond to those of the XY plane, i.e., the regions of fine equiaxed structures corresponded to the equiaxed regions on the XY plane, while the coarse columnar structures corresponded to the coarse elongated grains. It is known that two main stages are divided into the metal solidification process, that is, crystal nucleation and growth. A certain degree of undercooling is required for nucleation. Increasing the undercooling has a great effect on the nucleation rate and growth rate (Ref 39). Meanwhile, combining the theory of metal solidification under the laser energy source reported by Liu et al. (Ref 40), during the SLM process, the powders were fused into liquid after heating by laser, then the equiaxed solidification was accrued firstly at some degree of undercooling. Then, the number of grains remains constant. And the solidification proceeded firstly via the lengthening of
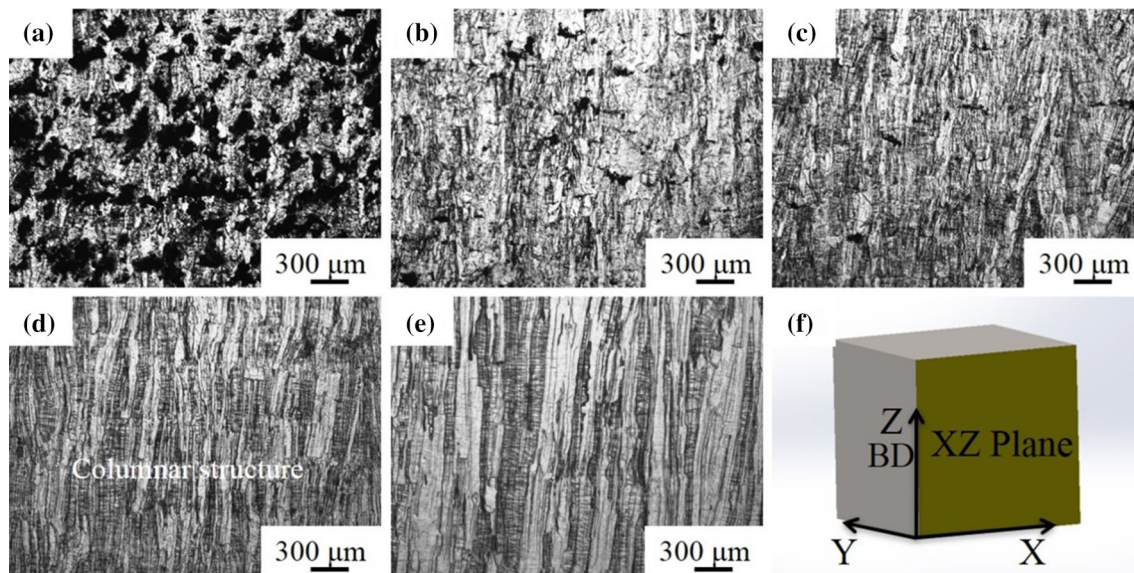
Fig. 7 OM images of the microstructures (XZ plane) the SLM specimens and 3D physical model of the sample. (a) 150 J/m, (b) 210 J/m, (c) 300 J/m, (d) 420 J/m, (e) 540 J/m, (f) 3D physical model of the sample

dendrites. Lower LED led to a lower temperature which resulted in un-melted particles and insufficient nucleation; thus, the dendritic phase or equiaxed grains were obtained. The LED was increased, which induced a completed melt of the powder in the molten layer. And the undercooling was also increased. Then, the new nucleation was almost formed; therefore, the initially equiaxed grains could still grow further. Finally, dendritic crystals were filled with liquid metal. Therefore, coarse columnar structures could be observed obviously in the SLM Fe-3wt.% Si alloys, instead of dendritic crystals. Besides, with a further increase in LED, a higher temperature was obtained. The movement of the atomic was also enhanced, which contributes to a further growth of the crystal. In the same situation, the formation of columnar structures was also further promoted. These result in columnar structures when the LED reached 300 J/m, and a gradual increase in size and number of columnar structures corresponding to the samples E420 and E540.

The representative SEM graphics of the side view XZ plane are presented in Fig. 8. The un-melted particles with a dendritic phase and the columnar structures are observed clearly, which further proves that the LED was impacted significantly on the microstructures as mentioned previously. Unfortunately, the feature of the molten pools cannot be distinguished clearly in this situation. The XZ planes of samples E300 and E540 are further enlarged to observe the section features of molten pools and columnar structures, and the results are shown in Fig. 9. It can be observed the boundaries of some molten pools (indicated by orange dotted lines) and the existing columnar grains grow across multiple molten pools. The molten pools are relatively wide and deep at high LED, which is one of the reasons for increasing the amount of coarse columnar structures.

3.2.3 Microhardness. The microhardness of SLM samples is significantly related to their internal microstructure. The results of the microhardness measurement (XY and XZ planes) for SLM Fe-3wt.% Si alloys under different laser energy densities are shown in the histogram in Fig. 10. In both XY and XZ planes, the microhardness value of each sample is higher than 200 $HV_{0.1}$. As a result of the inhomogeneous distribution of defects, the hardness of XY and XZ planes is slightly different. The microhardness value of the sample E150 is the lowest. And it is associated with the maximum number of un-melted particles and the highest porosity rate. The augmentation of the microhardness value of the corresponding samples is also related to the reduction in the porosity rate. Due to the largest reduction in porosity rate between the sample E150 and E210, the increasing extent of microhardness is also the largest. Then, the increasing extent of microhardness between the sample E150 and E210 is significant, although the microhardness changes slightly when the LED increases from 300 to 420 J/m. It should be noted the decrease in microhardness value when E = 420 up to E = 540 J/m. According to the previous analysis, the porosity rate of samples E420 and E540 was almost similar. Besides, the over-burning phenomenon and Marangoni effects appeared in sample E540, which leads to a decreasing in microhardness value (Ref 37, 41).

3.3 Magnetic Properties

3.3.1 Coercivity. Coercivity is an important criterion for determining whether a ferromagnetic material is soft or hard. One of the goals in the preparation of soft magnetic material is keeping coercivity at a minimum level. The variation of coercivity (Hc) of the original powder and the SLM Fe-3wt.% Si samples is displayed in Fig. 11 as a function of LED. The coercivity value of each sample was lower than that of the original powder. Although the fluctuation of Hc between different samples is not very strong, it could still be found that Hc decreases with increasing the LED when the LED is lower than 300 J/m. On the contrary, both Hc show an increase when the LED increases from 300 to 420 J/m and 500 J/m. Theoretically, the coercivity of material is usually related to the microstructural characteristics, including the defects; the shape, size, and dispersion degree of the grains and lattice distortion. And the internal stress also strongly impacts the
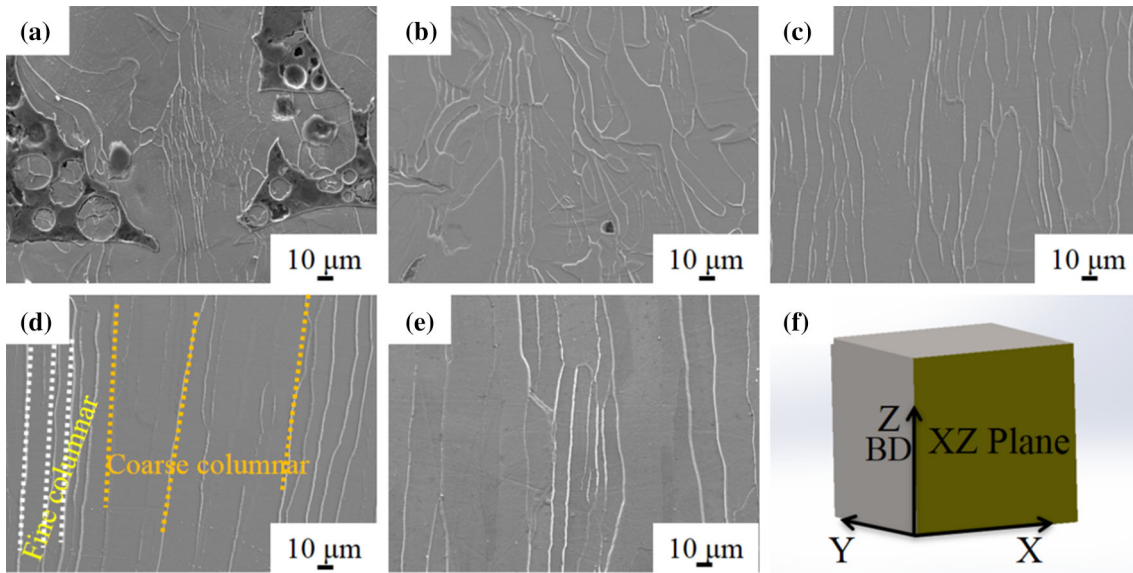
Fig. 8 SEM images of the microstructures (XZ plane) of the SLM specimens (a-e): (a): E150, (b): E210, (c): E300, (d): E420, (e): E540; The 3D physical model of the sample (f). SEM images of the microstructures (XZ plane) of SLM specimens at different LED and 3D physical model of the sample. (a) 150 J/m, (b) 210 J/m, (c) 300 J/m, (d) 420 J/m, (e) 540 J/m, (f) 3D physical model of the sample
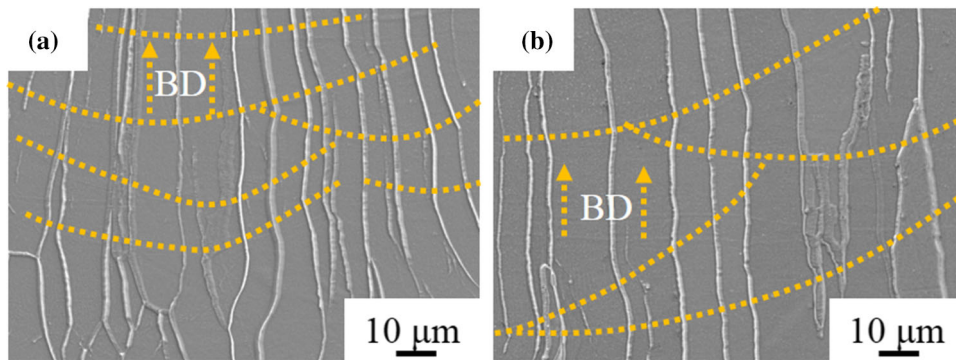

Fig. 9 SEM images of the enlarged view for representative microstructures (XZ plane) at different LEDs. (a) 300 J/m, (b) 540 J/m
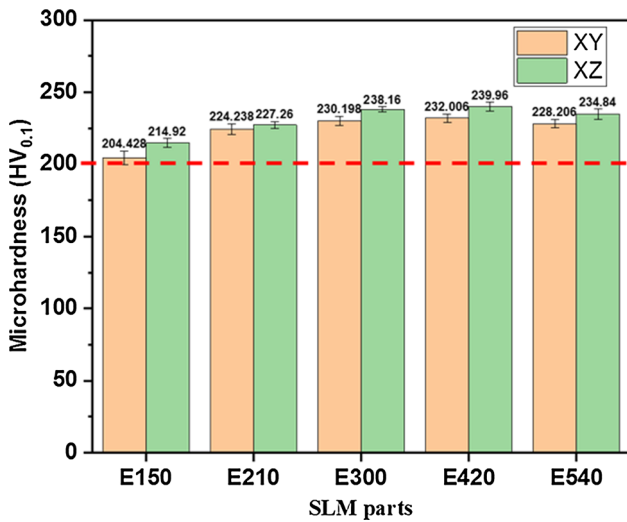

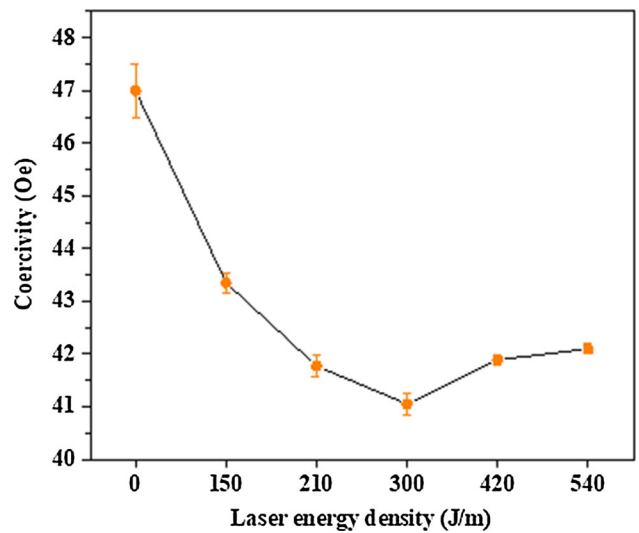**Fig. 10** Microhardness of the SLM parts prepared at the different LED

Fig. 11 The value of coercivity changes as a function of laser energy density

coercivity with a negative relationship. In fact, due to the irreversible movement of domain walls is responsible for the coercive force, manufacturing defects, such as porosity, cracks, and impurities, represent pinning sites obstructing the movement of the magnetic domain walls under the external magnetic field effect, increasing coercivity (Ref 17, 42). Additionally, the coercivity is inversely proportional to grain size for polycrystalline magnetic materials with grain sizes above 150 nm following the 1/D law (Ref 43, 44). Hence, a relatively higher value of Hc for the samples E150 could be attributed to the structural defects, including a relatively higher porosity rate and more un-melted particles. The reduction in Hc for SLM Fe-3wt.% Si samples when E = 150 J/m up to E = 300 J/m could be related to the reduction in porosity rate and the homogenous evolution of microstructure. Nevertheless, the increase in Hc when E = 300 up to E = 540 J/m could be associated with higher internal stress. It is known that the internal stress of the SLM samples using high LED is higher than that of using low LED (Ref 15). Thus, it could be indicated that while both coarsening of grains and increasing of internal stress could contribute to the magnetic behavior, the internal stress became the principal obstruction in a magnetic field when the LED is higher than 300 J/m.

    3.3.2 Saturation Magnetization. The saturation magnetization of the material corresponds to the limiting case that all atomic moments take the allowed angular position nearest to the field. The saturation magnetization is also a prominent structure-insensitive property (Ref 1, 42). The evolution of saturation magnetization (Ms) of the raw powder and SLM samples is given in Fig. 12. The Ms of all samples is higher than that of raw powder. With the increase in LED, Ms increases at first, reaching a maximum value of about 220 emu/g when the LED is 300 J/m and then decreases gradually. It is well known that the crystal eventually reaches saturation magnetization when all spins have rotated into the field direction (Ref 1). A relatively high porosity rate can lead to a relatively low saturation magnetization. So, the increase in Ms when E = 150 up to E = 300 J/m owing to the reduction in porosity. With the increase in temperature at E > 300 J/m, the ability of atom activity was promoted. The reduction in Ms is
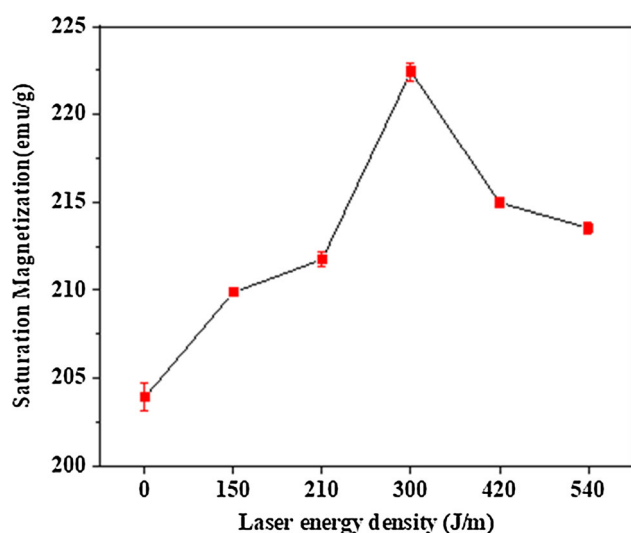
also related to the nearest-neighbor configuration of Fe atoms through their substitution by non-magnetic Si atoms, leading to the reduction in the magnetic moment per atom. It can be reasonably indicated that the magnetic properties of coercivity and saturation magnetization of SLM Fe-3wt.% Si alloy strongly depend on the parameters such as the number of defects, grain size, and internal stress.

    In this study, the investigation of the magnetic properties was mainly focused on coercivity and saturation magnetization. The saturation magnetization value (222.4 emu/g) of the prepared samples is higher than that of SLM FeSiB parts (199 emu/g) reported by Alleg et al. (Ref 19), and the lowest coercivity of the samples is 41.05 Oe which is lower than the value (43.8 Oe) in that report (Ref 19). It indicates that the SLM parts in our work exhibit better soft magnetic properties. The coercivity of the samples in this work is higher than the result (27 Oe) of the report (Ref 45), but the saturation magnetization is better than their result (91.8 emu/g). Although the comprehensive magnetic properties are still not matched with commercial requirements, the cracks do not exist on SLM parts of this work, and certain results are better than those reported in some related studies.

4. Conclusions

In this work, a series of Fe-3wt.% Si specimens were successfully prepared by SLM technology using metallurgical powder. The impact of LED on the surface morphology, surface roughness, microstructure of the selective laser melted Fe-3wt.% Si alloy was analyzed and described in detail. Summary conclusions are obtained from this investigation as follows:

1. The surface morphology of the corresponding SLM Fe-3wt.% Si alloy is improved by higher LED, which results in a low value of surface roughness. And the decrease in the porosity rate of corresponding specimens is related to the increase in LED.
2. The cross-sectional microstructure of SLM Fe-3wt.% Si parts is a typical columnar structure with an oriented growth of building direction. And the columnar structure at high LED is coarser than that at low LED.
3. The microhardness value of each SLM part is higher than 200 $HV_{0.1}$. The microhardness value of the corresponding samples when LED lower than 420 J/m increases accordingly. However, it is decreased when E = 420 up to E = 540 J/m due to the almost similar porosity, and the burning phenomenon and Marangoni effects in sample E540.
4. The coercivity of SLM specimens decreases first and then increases with the increase in LED, while the evolution of saturation magnetization and LED is opposite. The specimen with a LED at 300 J/m exhibits better comprehensive magnetic properties than other specimens. It can be concluded that the magnetic properties of coercivity and saturation magnetization of Fe-3wt.% Si alloy produced by SLM are affected by the LED, which can be attributed to the parameters such as the number of defects, grain size, etc.

This work demonstrates that the SLM LED has an obvious influence on the surface morphology and microstructure of the

Fig. 12 The value of saturation magnetization changes as a function of laser energy density

Fe-3wt.% Si. It can be concluded that the surface morphology and the microstructure are improved by using higher energy input. And this investigation also exhibits the potential possibility of three-dimensional Fe-Si soft magnetic alloys manufactured by SLM technology used in electromechanical applications.

Acknowledgments

References

1. G.E. Fish, Soft Magnetic Materials, *Proc. IEEE*, 1990, **78**, p 947–972

2. C.-W. Chen, Magnetism and Metallurgy of Soft Magnetic Materials, Courier Corporation, 2013

3. H. Shokrollahi and K. Janghorban, Soft Magnetic Composite Materials (SMCs), *J. Mater. Process. Technol.*, 2007, **189**, p 1–12

4. K.I. Arai and K. Ishiyama, Rolled Texture and Magnetic Properties of 3% Silicon Steel, *J. Appl. Phys.*, 1988, **64**, p 5352–5354

5. J.S. Robles, A.S. Zamarripa, M.G. Mata and J. Cabrera, Texture Evolution of Experimental Silicon Steel Grades Part I: Hot rolling, *J. Magn. Magn. Mater.*, 2017, **429**, p 367–371

6. P. Jang, B. Lee and G. Choi, Effects of Annealing on the Magnetic Properties of Fe–6.5% Si Alloy Powder Cores, *J. Appl. Phys.*, 2008, **103**, p 07E743

7. S. Hong-Yu, H.-T. Liu, H.-H. Lu, H.-Z. Li, W.-Q. Liu, X.-M. Zhang and G.-D. Wang, Effect of Hot Rolling Reduction on Microstructure, Texture and Ductility of Strip-Cast Grain-Oriented Silicon Steel with Different Solidification Structures, *Mater. Sci. Eng. A*, 2014, **605**, p 260–269

8. X. He, X. Li and Y. Sun, Microstructure and Magnetic Properties of High Silicon Electrical Steel Produced by Electron Beam Physical Vapor Deposition, *J. Magn. Magn. Mater.*, 2008, **320**, p 217–221

9. X. Yan, C. Huang, C. Chen, R. Bolot, L. Dembinski, R. Huang, W. Ma, H. Liao and M. Liu, Additive Manufacturing of WC Reinforced Maraging Steel 300 Composites by Cold Spraying and Selective Laser Melting, *Surf. Coat. Technol.*, 2019, **371**, p 161–171

10. I. Gibson, D.W. Rosen and B. Stucker, *Additive Manufacturing Technologies*, Springer, New York, 2014

11. X. Yan, S. Yin, C. Chen, C. Huang, R. Bolot, R. Lupoi, M. Kuang, W. Ma, C. Coddet and H. Liao, Effect of Heat Treatment on the Phase Transformation and Mechanical Properties of Ti6Al4V Fabricated by Selective Laser Melting, *J. Alloys Compd.*, 2018, **764**, p 1056–1071

12. A. Uriondo, M. Esperon-Miguez and S. Perinpanayagam, The Present and Future of Additive Manufacturing in the Aerospace Sector: A Review of Important Aspects. Proc, *Inst. Mech Eng. G. J. Aerosp Eng.*, 2015, **229**, p 2132–2147

13. M. Garibaldi, C. Gerada, I. Ashcroft, R. Hague, H. Morvan, The impact of additive manufacturing on the development of electrical machines for MEA Applications: A feasibility study, in MEA2015 More Electric Aircraft, 2015

14. B. Zhang, N.-E. Fenineche, H. Liao and C. Coddet, Magnetic Properties of In-Situ Synthesized FeNi3 by Selective Laser Melting Fe–80% Ni Powders, *J. Magn. Magn. Mater.*, 2013, **336**, p 49–54

15. B. Zhang, N.-E. Fenineche, H. Liao and C. Coddet, Microstructure and Magnetic Properties of Fe–Ni Alloy Fabricated By Selective Laser Melting Fe/Ni Mixed Powders, *J. Mater. Sci. Technol.*, 2013, **29**, p 757–760

16. C. Mikler, V. Chaudhary, V. Soni, B. Gwalani, R. Ramanujan and R. Banerjee, Tuning the Phase Stability and Magnetic Properties of Laser Additively Processed Fe-30at% Ni Soft Magnetic Alloys, *Mater. Lett.*, 2017, **199**, p 88–92

17. M. Garibaldi, I. Ashcroft, N. Hillier, S. Harmon and R. Hague, Relationship Between Laser Energy Input, Microstructures and Magnetic Properties of Selective Laser Melted Fe-6.9% wt Si Soft Magnets, *Materials Characterization.*, 2018, **143**, p 144–151

18. M. Garibaldi, I. Ashcroft, M. Simonelli and R. Hague, Metallurgy of High-Silicon Steel Parts Produced using Selective Laser Melting, *Acta Mater.*, 2016, **110**, p 207–216

19. S. Alleg, R. Drablia and N. Fenineche, Effect of the Laser Scan Rate on the Microstructure, Magnetic Properties, and Microhardness of Selective Laser-Melted FeSiB, *J. Supercond. Novel Magn.*, 2018, **31**, p 3565–3577

20. A. Plotkowski, J. Pries, F. List, P. Nandwana, B. Stump, K. Carver and R. Dehoff, Influence of Scan Pattern and Geometry on the microsTructure and Soft-Magnetic Performance of Additively Manufactured Fe-Si, *Addit. Manuf.*, 2019, **29**, p 100781

21. S. Liu, J. Liu, J. Chen and X. Liu, Influence of Surface Tension on the Molten Pool Morphology in Laser Melting, *Int. J. Therm. Sci.*, 2019, **146**, p 106075

22. C. Ma and D. Bothe, Direct Numerical Simulation of Thermocapillary Flow Based on the Volume of Fluid Method, *Int. J. Multiphase Flow*, 2011, **37**, p 1045–1058

23. M. Guo, D. Gu, L. Xi, H. Zhang, J. Zhang, J. Yang and R. Wang, Selective Laser Melting Additive Manufacturing of Pure Tungsten: Role of Volumetric Energy Density on Densification, Microstructure and Mechanical Properties, *Int. J. Refract. Met. Hard Mater*, 2019, **84**, p 105025

24. J. Yi, J. Kang, T. Wang, X. Wang, Y. Hu, T. Feng, Y. Feng and P. Wu, Effect of Laser Energy Density on the Microstructure, Mechanical Properties, and Deformation of Inconel 718 Samples Fabricated by Selective Laser Melting, *J. Alloys Compd.*, 2019, **786**, p 481–488

25. M.H. Nasab, D. Gastaldi, N.F. Lecis and M. Vedani, On Morphological Surface Features of the Parts Printed by Selective Laser Melting (SLM), *Addit. Manuf.*, 2018, **24**, p 373–377

26. D. Gu and Y. Shen, Balling Phenomena in Direct Laser Sintering of Stainless Steel Powder: Metallurgical Mechanisms and Control Methods, *Mater. Des.*, 2009, **30**, p 2903–2910

27. G. Dursun, S. Ibekwe, G. Li, P. Mensah, G. Joshi and D. Jerro, Influence of Laser Processing Parameters on the Surface Characteristics of 316L Stainless Steel Manufactured by Selective Laser Melting, *Mater. Today: Proc.*, 2020, **26**, p 387–393

28. G. Ng, A. Jarfors, G. Bi and H. Zheng, Porosity Formation and Gas Bubble Retention in Laser Metal Deposition, *Appl. Phys. A*, 2009, **97**, p 641–649

29. R. Xiao and X. Zhang, Problems and Issues in Laser Beam Welding of Aluminum–Lithium Alloys, *J. Manuf. Processes*, 2014, **16**, p 166–175

30. N.T. Aboulkhair, N.M. Everitt, I. Ashcroft and C. Tuck, Reducing Porosity in AlSi10Mg Parts Processed by Selective Laser Melting, *Addit. Manuf.*, 2014, **1**, p 77–86

31. M. Xia, D. Gu, G. Yu, D. Dai, H. Chen and Q. Shi, Porosity Evolution and its Thermodynamic Mechanism of Randomly Packed Powder-Bed During Selective Laser Melting of Inconel 718 Alloy, *Int. J. Mach. Tools Manuf.*, 2017, **116**, p 96–106

32. C. Qiu, C. Panwisawas, M. Ward, H.C. Basoalto, J.W. Brooks and M.M. Attallah, On the Role of Melt Flow into the Surface Structure and Porosity Development During Selective Laser Melting, *Acta Mater.*, 2015, **96**, p 72–79

33. M. Boivineau, C. Cagran, D. Doytier, V. Eyraud, M.-H. Nadal, B. Wilthan and G. Pottlacher, Thermophysical Properties of Solid and Liquid Ti-6Al-4V (TA6V) Alloy, *Int. J. Thermophys.*, 2006, **27**, p 507–529

34. B. Zhang, Y. Li and Q. Bai, Defect Formation Mechanisms in Selective Laser Melting: A Review, *Chin J Mech Eng*, 2017, **30**, p 515–527

35. W. Yuan, H. Chen, T. Cheng and Q. Wei, Effects of Laser Scanning Speeds on Different States of the Molten Pool During Selective Laser Melting: Simulation and Experiment, *Mater. Des.*, 2020, **189**, p 108542

36. E.O. Olakanmi, R. Cochrane and K. Dalgarno, A Review on Selective Laser Sintering/Melting (SLS/SLM) of Aluminium Alloy Powders: Processing, Microstructure, and Properties, *Prog. Mater Sci.*, 2015, **74**, p 401–477

37. L. Tonelli, A. Fortunato and L. Ceschini, CoCr Alloy Processed by Selective Laser Melting (SLM): Effect of Laser Energy Density on Microstructure, Surface Morphology, and Hardness, *J. Manuf. Processes*, 2020, **52**, p 106–119

38. T. Niendorf, S. Leuders, A. Riemer, H.A. Richard, T. Tröster and D. Schwarze, Highly Anisotropic Steel Processed by Selective Laser Melting, *Metall. Mater. Trans. B*, 2013, **44**, p 794–796

39. D. Stefanescu, R. Ruxanda, Fundamentals of Solidification ed: ASM International 2004, p 71-92
40. S. Liu, Y. Li, F. Liu, H. Zhang and H. Ding, Effects of relative Positioning of Energy Sources on Weld Integrity for Hybrid Laser arc Welding, *Opt. Lasers Eng.*, 2016, **81**, p 87–96
41. S.L. Sing, F.E. Wiria and W.Y. Yeong, Selective Laser Melting of Titanium Alloy with 50 wt.% Tantalum: Effect of Laser Process Parameters on Part Quality, *Int. J. Refract. Met. Hard Mater*, 2018, **77**, p 120–127
42. R. Hilzinger, W. Rodewald, Magnetic materials: fundamentals, products, properties, applications, Vacuumschmelze, 2013
43. F. Pfeifer and C. Radeloff, Soft Magnetic Ni-Fe and Co-Fe Alloys-Some Physical and Metallurgical Aspects, *J. Magn. Magn. Mater.*, 1980, **19**, p 190–207
44. G. Ouyang, X. Chen, Y. Liang, C. Macziewski and J. Cui, Review of Fe-6.5 wt.%Si High Silicon Steel—A Promising Soft Magnetic Material for sub-kHz Application, *J. Magn. Magn. Mater.*, 2019, **481**, p 234–250
45. N. Kang, M. El Mansori, F. Guittonneau, H. Liao, Y. Fu and E. Aubry, Controllable Mesostructure, Magnetic Properties of Soft Magnetic Fe-Ni-Si by Using Selective Laser Melting from Nickel Coated High Silicon Steel Powder, *Appl. Surf. Sci.*, 2018, **455**, p 736–741